Soft Matter

Accepted Manuscript

This article can be cited before page numbers have been issued, to do this please use: M. A. Quetzeri-Santiago, I. Hunter, D. van der Meer and D. Fernandez Rivas, *Soft Matter*, 2021, DOI: 10.1039/D1SM00706H.

ROYAL SOCIETY OF CHEMISTRY

rsc.li/soft-matter-journal

View Article Online
DOI: 10.1039/D1SM00706H

Soft Matter

ARTICLE TYPE

Cite this: DOI: 00.0000/xxxxxxxxxx

Impact of a microfluidic jet onto a pendant droplet†

Miguel A. Quetzeri-Santiago,*[a] Ian W. Hunter,[b] Devaraj van der Meer, [c] and David Fernandez Rivas‡[a,c]

Received Date
Accepted Date

DOI: 00.0000/xxxxxxxxxx

High speed microfluidic jets can be generated by a thermocavitation process: from the evaporation of the liquid inside a microfluidic channel, a rapidly expanding bubble is formed and generates a jet through a flow focusing effect. Here, we study the impact and traversing of such jets on a pendant liquid droplet. Upon impact, an expanding cavity is created, and, above a critical impact velocity, the jet traverses the entire droplet. We predict the critical traversing velocity (i) from a simple energy balance and (ii) by comparing the Young-Laplace and dynamic pressures in the cavity that is created during impact. We contrast the model predictions against experiments, in which we vary the liquid properties of the pendant droplet and find good agreement. In addition, we asses how surfactants and viscoelastic effects influence the critical impact velocity. Our results increase the knowledge of the jet interaction with materials of well known physical properties.

1 Introduction

The impact of a solid or liquid object into a deep liquid pool generates a cavity with dynamics first described by A.M. Worthington in 1908[1]. Since then, research has focused on many topics, including the critical energy necessary for air entrainment into the pool, the collapse of the formed cavity, and the subsequent formation of Worthington jets[2–7]. The projectiles studied in the literature usually have sizes in the range of 1 to 5 mm, an impact speed range of 1 to 10 m/s, and the pool is usually orders of magnitude larger than the projectile and the created cavity[2–7]. In these cases, hydrostatic pressure has been found a major driver for the collapse and retraction of the cavity made on the liquid pool[2]. In contrast, we found just two works discussing the impact of projectiles in the submillimeter range[8,9]. In this paper we study for the first time the impact of micrometer-sized jets ($\approx 100\ \mu$m) onto a self-contained liquid object, namely droplets of ≈ 2 mm. In this case, the jets travelling at speeds of ≈ 20 m/s generate a cavity circumscribed by the droplet volume and the hydrostatic pressure can be neglected.

Since, the dynamics of the aforementioned events take place in a few miliseconds, high-speed imaging is required to observe the phenomena. High-speed imaging was pioneered by scientists like Harold E. Edgerton, with his strobe-flash photography technique[10]. One of his most famous sequences of pictures is that of a 0.22 inch caliber bullet traversing an apple at ≈ 500 m/s (Fig. 1a). In this sequence, the apple is opaque, but, what if we could replace the target with a transparent object, i.e., a *liquid apple*? This is precisely the case when we target a droplet with a liquid microjet. As shown in Fig. 1, the aesthetic of a high-speed jet traversing a liquid droplet and Edgerton's pictures is strikingly similar. The difference being that, with a translucent liquid, we can observe the impact dynamics inside the droplet, and besides producing impressive images, high-speed imaging facilitates the description of the fast phenomena, such as providing the projectile speed and the target deformation.

Our aim in this paper is to unravel the physics that govern the impact of liquid water jets on a pendant droplet of liquids with different properties. This knowledge increases our understanding of the jet interaction with materials of well known physical properties. Such understanding can advance our knowledge on needle-free injections, because jets of similar sizes and speeds to the present study have been proposed for that purpose[11–13].

The paper is structured as follows. The experimental procedure is outlined in §2. In §3 we present two models to predict the critical jet velocity for traversing a droplet: In §3.1 we use an energy balance between the kinetic energy of the jet and the surface energy of the droplet. In §3.2, we employ the two-dimensional Rayleigh equation to obtain the cavity shape and combine it with the Young-Laplace equation to predict its collapse. Next, the model prediction is contrasted against experimental results in §4.1. Additionally, in §4.2 and §4.3 we present

[a]Mesoscale Chemical Systems Group, MESA+ Institute and Faculty of Science and Technology, University of Twente, P.O. Box 217, 7500AE Enschede, The Netherlands; E-mail: m.a.quetzerisantiago@utwente.nl
[b]BioInstrumentation Laboratory, Department of Mechanical Engineering, Massachusetts Institute of Technology, Cambridge, Massachusetts 02139, USA
[b]BioInstrumentation Laboratory, Department of Mechanical Engineering, Massachusetts Institute of Technology, Cambridge, Massachusetts 02139, USA
† Electronic Supplementary Information (ESI) available: [details of any supplementary information available should be included here]. See DOI: 10.1039/cXsm00000x/
‡E-mail: d.fernandezrivas@utwente.nl

View Article Online
DOI: 10.1039/D1SM00706H

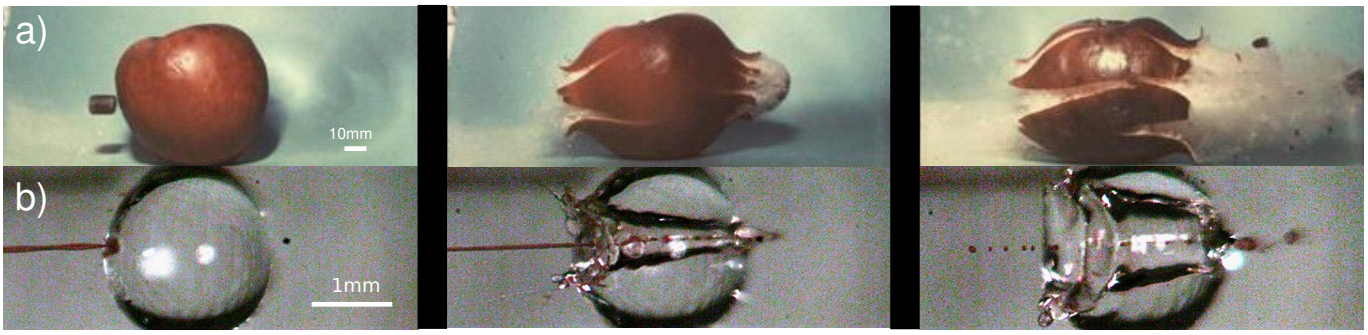

Fig. 1 Comparison between a sequence of images from, a) Harold E. Edgerton, Bullet through Apple, 1964, $U_{bullet} \sim 500$ m/s (reprinted with the permission of James W. Bales and Andrew Davidhazy). The sequence is taken using the flash photography technique[10], with a flash duration of $\approx 1/3$ μs. The flash is triggered by an electronic circuit that reacts to the sound of the rifle shot. b) The impact of a liquid jet on a droplet; the video is recorded with a high-speed camera at 50k frames per second, the jet diameter is $D_{jet} = 100$ μm and its impact velocity is $U_{jet} = 25.8$ m/s (see also movie 1 in the supplementary material). Apart from the striking aesthetic resemblance of the processes, the ratio between the projectile kinetic energy and the energy associated with the target's resistance to deformation is on the same order of magnitude, see Section §3.1.

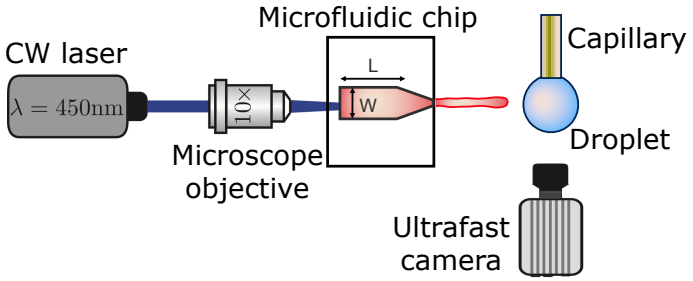

Fig. 2 Schematic of the experimental setup. Thermocavitation is obtained focusing a CW laser at the bottom of a microfluidic device with a microscope objective. The thermocavitated bubble expands and creates a liquid jet that is directed to a pendant droplet. The process is recorded with a high-speed camera with the illumination coming from a light source from the front so the cavity evolution can be observed.

experimental results on the cavity advancing and retracting velocities with some observations on what occurs after the cavity collapse.

2 Experimental Method

High-speed jets were generated from a thermocavitation process and directed to impact a pendant droplet of different liquids with varying properties. Thermocavitation refers to the phenomena where a liquid is vaporised locally by means of a focused laser, leading to bubble nucleation[14,15]. The expansion of the nucleated bubble can be controlled on a microfluidic chip to generate a jet through a flow-focusing effect[16,17]. These jets may reach speeds in the order of 100 m/s, which, is enough to pierce the skin, and has potential for transdermal delivery of a liquid, particularly needle-free injections[18,19]. However, in the experiments described here, we restrict the jet velocity U_{jet} to the range of 8 - 35 m/s, which is sufficient for a jet to traverse droplets of the liquids studied. Additionally, the diameter of the liquid jet was in the range of D_{jet} = 50 - 120 μm. Both U_{jet} and D_{jet} were controlled by varying the laser spot size and power.

The experimental setup is shown in Fig. 2. A Borofloat glass microfluidic chip fabricated under cleanroom conditions is filled with a water solution containing a red dye (Direct Red 81, CAS No. 2610-11-9) at 0.5 wt. %. The red dye enhances the laser energy absorption and facilitate the bubble nucleation. The microfluidic device has a tapered channel with an angle $\alpha = 15$ degrees to avoid swirling of the jet[17], nozzle diameter $d = 120$ μm, channel length $L = 1050$ μm and width $W = 600$ μm. The thermocavitation bubble is created by focusing a continuous wave laser diode (Roithner LaserTechnik, wavelength $\Lambda = 450$ nm and nominal power of 3.5 W), at the microchannel with a 10x microscope objective. The liquids used were water, ethanol, aqueous solutions of glycerol, Triton x-100 and sodium-bis(2-ethylhexyl)sulfosuccinate (Aerosol OT) at different concentrations and polyethylene-oxide of varied molecular weight (PEO). Liquid droplets were created by holding a capillary tube with outer diameter of 360 μm, controlling the volume with a precision glass syringe and a syringe pump (Harvard PHD 22/2000). All chemical additives were bought from Sigma-Aldrich. The properties of the Newtonian and non-Newtonian liquids used are reported in table 1. The surface tension of all the liquids was measured with the Pendent Drop ImageJ plugin[20], and their shear viscosity with an Anton Paar MCR 502 rheometer.

The processes of bubble generation, jet ejection and impact on the liquid droplet were recorded with a Photron Fastcam SAX coupled with a 2x microscope objective. A typical experiment duration was ~ 5 ms and the camera resolution was set to 768×328 pixels^2 at a sample rate of 50k frames per second with an exposure time of 2.5 μs. Typical images obtained from the experiments are shown in Fig. 3, where one observes how a water droplet is pierced by the liquid jet produced from the microchip on the left, using shadowgraph imaging (left) and direct lighting (right). Experiments were carried out with a typical shadowgraph configuration, and we switched to a front light illumination system to observe the cavity dynamics. In the front illumination system a white background was placed to enhance image contrast and increase the light reaching the camera sensor. Image analysis to extract the jet diameter, impact velocity and cavity dynamics was performed with a custom generated MATLAB script. The shadowgraph imaging benefits from more light reaching the sensor, and thus a smaller camera exposure time can be used, leading to

View Article Online
DOI: 10.1039/D1SM00706H

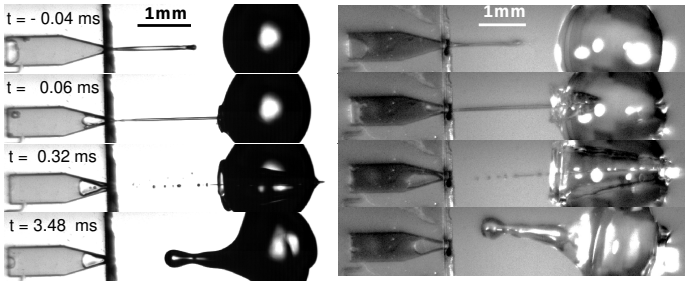

Fig. 3 Snapshot sequences of a jet impacting on a water droplet with Triton X-100 at 3 CMC (left, movie 2 in the supplementary materials) and a pure water droplet (right, movie 3 in the supplementary materials). In the former $U_{jet} = 16.3$ m/s, $We_{jet} = 654$ and $D_{drop} = 1.65$ mm. In the latter $U_{jet} = 17.1$ m/s, $We_{jet} = 325$ and $D_{drop} = 1.86$ mm. The imaging of the left sequence is done with a conventional shadowgraph illumination system. In contrast, the right sequence is taken with a front light illumination system, where the cavity dynamics can be more clearly observed. Times are taken relative to the impact moment at $t = 0$. The impact process is qualitatively the same for both of the droplets; a cavity is generated inside the droplet (t $\sim$ 0.06 ms), the jet traverses the droplet (t $\sim$ 0.032 ms) and a rebound Worthington jet is generated (t $\sim$ 3.48 ms). Time is taken from the impact moment t = 0 ms.

a better jet definition. However, extracting information from the expanding cavity is impossible. In contrast, with front light imaging we can extract the information from the expanding cavity, but the jet is not as well defined as with shadowgraphy.

3 Critical jet velocity

In this section, we predict the critical velocity needed for a jet to traverse a droplet using two different approaches, (i) by using a simple energy balance and (ii) by comparing the Young-Laplace and dynamic pressures in the cavity that is created during impact. In §3.1, we start from an energy analysis of Edgerton's experiment of a bullet traversing an apple and subsequently transfer the argument to the droplet case of our current study. With this example we introduce the concept of kinetic energy of the projectile and the resistance of the target to being traversed. Moreover, we deduce the critical velocity of the jet by doing an energy balance between the kinetic energy of the jet and the surface energy of the droplet. Additionally, in §3.2, we use the Rayleigh's two dimensional equation to predict the shape of the cavity and predict its collapse with the Young-Laplace equation, thus finding the jet critical traversing velocity.

3.1 Energy balance between the jet kinetic energy and the droplet surface energy

In his lecture titled *How to Make Applesauce at MIT*, Edgerton presented his famous series of pictures of bullets traversing apples presented in Fig. 1a. This set of images illustrated the traversing process, but did not reflect on the energy of the bullet or the energy of the apple. What would it take the apple to stop the bullet? Or equivalently, what would be the necessary speed for the bullet to get *trapped* and *embeded* inside the apple?

In this section, we will answer these questions by using an energy balance between the kinetic energy of a bullet $E_{k_{bullet}} = M_{bullet}U_{bullet}^2/2$, where M_{bullet} is the mass of the bullet, and the toughness of an apple T_{apple}, which we define as its ability to absorb energy by elastoplastic deformation without fracturing. Hence, by doing the energy balance, the critical velocity for the bullet to penetrate the apple may be written as

$$U^*_{bullet} = \sqrt{2T_{apple}/M_{bullet}}. \quad (1)$$

Since we considered that the whole apple absorbs all the energy of the bullet impact, we remark that the energy balance is valid just when the diameter of the bullet has a similar size to that of the apple. The mass of a .22 caliber bullet is $M_{bullet} \approx 10$ g and the apple toughness is $T_{apple} \approx 10$ J[21]. Therefore, $U^*_{bullet} \approx 45$ m/s, which is at least one order of magnitude smaller than the typical velocities reached by .22 caliber bullets, $U_{bullet} \approx 380$ m/s[22]. Consequently, it is understandable that the apple is traversed by the bullet in Edgerton's photographs.

For our liquid jet, the kinetic energy is $E_{k_{jet}} \approx (\pi/8)\rho_{jet}U_{jet}^2D_{jet}^2H_{jet}$, with ρ_{jet} and H_{jet} the density and length of the jet respectively, and the resisting force of the droplet is dominated by its surface energy. For the critical conditions where the jet traverses the droplet, the jet kinetic energy transforms into the surface energy of the cavity generated at impact. For simplicity, assuming that the cavity geometry is cylindrical, the cavity surface energy is $E_{\gamma_c} \approx \pi D_c D_{drop}\gamma_{drop}$, with γ_{drop} the droplet surface tension and D_c the cavity diameter. Here, D_c is constrained by D_{drop} and as shown in Figs. 3 and 4, $D_c \sim D_{drop}$. Also, since the velocity of the tip of the cavity is approximately half the jet velocity $U_c \approx \frac{1}{2}U_{jet}$, the total length of the jet would not contribute to the traversing process but only a part of it, namely $H^*_{jet} \approx 2D_{droplet}$[8]. Using this limiting value H^*_{jet}, the jet critical velocity for droplet traversing is

$$U^\dagger_{jet} \sim \left(\frac{\gamma_{drop}D_{drop}}{\rho_{jet}D_{jet}^2}\right)^{1/2}. \quad (2)$$

Defining the relevant Weber number of the jet as $We_{jet} = \rho_{jet}U_{jet}^2D_{jet}/\gamma_{drop}$, and substituting in equation 2 we find the critical minimal Weber number needed to traverse the droplet

$$We^\dagger_{jet} \sim \frac{D_{drop}}{D_{jet}}. \quad (3)$$

Substituting typical values of a jet impacting a water droplet in our experiments ($\rho_{jet} \approx 1000$ kg/m^3, $D_{jet} \approx 100$ μm $D_{drop} \approx 2$ mm and $\gamma_{drop} \approx 0.07$ mN/m), we obtain $U^\dagger_{jet} \approx 4$ m/s or $We^\dagger \approx 20$.

Now, we have all the ingredients to do a scaling comparison between a bullet traversing an apple and a jet traversing a droplet. Taking the values of U_{jet} and U_{bullet} from the experiments in Fig. 1a) and 1b (which are well above the critical value for penetration in both cases) and the target toughness (toughness for an apple and surface energy for a droplet), we get that $E_{k_{bullet}}/T_{apple} \sim E_{k_{jet}}/E_{\gamma_c} \sim 100$. Therefore, the relative energies involved in both processes are of the same order of magnitude, indicating that the traversing phenomena in both cases share more than aesthetic similarities. As both processes are in a regime dominated by inertia, we expect that the cavity creation follows similar physics. Indeed, in the context of shaped charges, the penetration of a solid onto another solid has been described from

View Article Online
DOI: 10.1039/D1SM00706H

Table 1 List of fluids used providing their shear viscosity μ, surface tension γ and density ρ. The viscoelastic relaxation time λ is also shown for the polyethylene-oxide solutions

Fluid	μ (mPa s)	γ (mN/m)	ρ (kg/m^3)	λ (ms)
Ethanol	1.04	26.3	789	-
Water	1.0	72.1	998	-
Aqueous Glycerol 25 v%	2.4	69.7	1071	-
Aqueous Glycerol 50 v%	8.4	67.6	1142	-
Aqueous Glycerol 70 v%	28.7	66.1	1193	-
Aqueous Glycerol 78 v%	43.6	65.2	1212	-
Triton 0.2 CMC%	1.0	43.9	998	-
Triton 1 CMC%	1.0	30.8	998	-
Triton 3 CMC%	1.0	32.5	998	-
Aerosol OT 1 wt.% (AOT 1%)	1.0	23.4	998	-
Aerosol OT 0.1 wt.% (AOT 0.1%)	1.0	24.1	998	-
Water & red dye 0.5 wt.%	0.91	47.0	1000	-
PEO 100k 0.1 wt%	1.03	63.2	996	0.006
PEO 100k 1 wt%	2.43	62.9	995	0.047
PEO 100k 10 wt%	50.8	62.5	1001	0.333
PEO 600k 0.1 wt%	1.56	63.1	996	0.307
PEO 600k 1 wt%	21.7	62.9	998	1.317

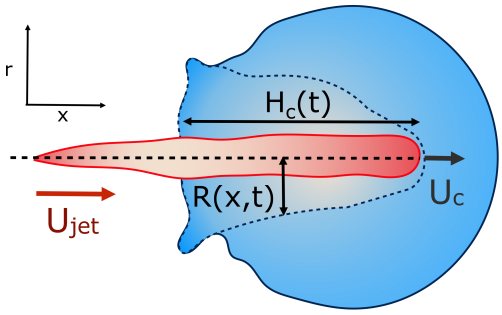

Fig. 4 Diagram illustrating the parameters used in this section. The jet impacts the pendant droplet from the left with velocity U_{jet}, creating a cavity with increasing depth in time $H_c(t)$, where the velocity of the apex of the cavity is indicated by $U_c = \dot{H}_c$ and whose radius depends on time and the position $R(x,t)$. Here, x is the direction along which the jet travels and r is its perpendicular radial direction.

the fluid dynamics perspective[23]. Nevertheless, after impact, the apple fractures and does not possess the restoring force a liquid droplet has, namely, the surface tension. This leads to a large discharge of mass at the back of the apple, with a cavity bigger at the exit point than at the entry point. In contrast, the droplet can redistribute its mass without breaking and the surface cavity closes due to the surface tension. This is the cause of the much appreciated fact that we did not have to deal with substantial amounts of debris after our experiments.

3.2 Comparison between the Young-Laplace and dynamic pressures of the cavity

Considering the mass of a cylindrical liquid jet with radius R_{jet} and length H_{jet} falling into a pool of the same liquid, air is entrained in the pool at sufficiently energetic impacts, i.e., $We >> 1$ and $Re >> 1$[2]. Additionally, the cavity dynamics and the air entrainment depend on the aspect ratio of the jet. The limiting cases are $H_{jet}/R_{jet} \to \infty$, corresponding to the impact of a continuous jet, and $H_{jet}/R_{jet} \to 1$, where the case of a droplet impact into a liquid pool is recovered[2,24]. For the former case, the apex of the cavity advances with a velocity $U_c = \frac{1}{2}U_{jet}$, therefore, the depth of the cavity can be estimated as $H_c = \frac{1}{2}U_{jet}t$[2,8,9].

In the cavity formation of a droplet impacting a liquid surface, the process is mainly inertial during the first instants, with surface tension becoming important at the moment near the maximum depth of the cavity H_{max}[8]. Additionally, Deng *et al.* in 2007[25] showed that viscous dissipation accounts for ~ 1.4 % of the initial kinetic energy loss of a water droplet of $D = 2.5$ mm impacting a liquid pool. Therefore, assuming that the cavity shape is slender and the process is inertia dominated, i.e., neglecting viscous dissipation, we can apply the two-dimensional Rayleigh equation in cylindrical coordinates to predict the cavity shape[26,27],

$$\left(R\frac{d^2R}{dt^2} + \left(\frac{dR}{dt}\right)^2\right)\log\frac{R}{R_\infty} + \frac{1}{2}\left(\frac{dR}{dt}\right)^2 \approx \frac{\gamma}{\rho R}, \tag{4}$$

where $R(x,t)$, is the radius of the cavity and x is the position of the cavity on the horizontal direction and R_∞ is an external length scale (see Fig. 4). Following the argument of Bouwhuis *et al.*[8], during the first instants of the cavity formation, inertia dominates and the dynamics are determined by $R(d^2R/dt^2) + (dR/dt)^2 \approx 0$. Solving this equation we get that $R(t) \sim (t - t_0)^{1/2}$, where $t = H_c/U_c$ and $t_0 = x/H_c$, and the approximate cavity profile is[8],

$$R(x,t) \approx \sqrt{\frac{D_{jet}}{2}(H_c - x)} = \sqrt{\frac{D_{jet}}{2}(U_c t - x)}. \tag{5}$$

The time t_c at which surface tension can influence the cavity walls can be predicted by comparing the dynamic pressure of the radially expanding cavity and the Young-Laplace pressure based on the azimuthal curvature of the cavity,

$$\rho\left(\frac{dR_{x=0}}{dt}\right)^2 \approx \frac{2\gamma}{R_{x=0}}, \tag{6}$$

where $R_{x=0} = R(0,t)$ is the cavity radius at the jet impact point $x = 0$. Taking the cavity profile from equation 5, we get $R_{x=0}(t) = \sqrt{1/2}\sqrt{D_{jet}U_c t}$, and $dR_{x=0}/dt \approx D_{jet}U_c/2^{3/2}\sqrt{D_{jet}U_c t}$[8]. Therefore,

View Article Online
DOI: 10.1039/D1SM00706H

$$t_c \approx \frac{\rho_{jet}^2 D_{jet}^3 U_c^3}{128\gamma_{drop}^2}, \tag{7}$$

and

$$H_{max} \approx U_c t_c. \tag{8}$$

The condition for the jet to traverse the droplet is that $D_{drop} < H_{max}$. Using that $U_c \approx \frac{1}{2}U_{jet}$ and equations 7 and 8, the critical impact velocity for the jet to traverse the droplet is

$$U_{jet}^* \approx 8\left(\frac{\gamma_{drop}^2 D_{drop}}{2\rho_{jet}^2 D_{jet}^3}\right)^{1/4}, \tag{9}$$

and

$$We_{jet}^* \approx 64\left(\frac{D_{drop}}{2D_{jet}}\right)^{1/2}. \tag{10}$$

For a jet impacting a water droplet, $D_{drop} = 2$ mm, $\gamma_{drop} = 0.072$ N/m, $D_{jet} = 100$ μm and $\rho_{jet} = 1000$ kg/m^3, we obtain that the critical velocity needed to traverse the droplet is $U_{jet}^* \approx 12$ m/s, which is $\sim 40\%$ larger than U_{jet}^* obtained from equation (2). Similarly, $We^* \approx 200$ which is about twice as large as for equation (3).

While the results in equations (3) and (10) are of the same order of magnitude, their dependence on the ratio D_{drop}/D_{jet} is different, namely linear in equation (3) whereas in equation (10), there is a square root dependence. This discrepancy arises from the difference in the geometric shape of the generated cavity that was assumed in the two approaches, resulting in a different surface energy. Indeed, a very simple cylindrical geometry was assumed during the energy balance method. In contrast, deriving equation (10) using the Rayleigh equation, leads to a more rigorous description of the cavity shape. Therefore, we consider the latter model to be more accurate and in the following section will compare our experimental data to equation (10).

4 Results and discussion

In this section we will describe our experiments on the traversing of the jet through the droplet and compare them to the above criterion. Furthermore, we modify the criterion to include the concept of dynamic surface tension of the droplet γ_{dyn} in the case of surfactant covered droplets. After that we will briefly discuss the cavity dynamics, focusing on the motion of the apex of the cavity inside the droplet. Finally, we comment on our observations for droplets containing surfactants and non-Newtonian liquids.

4.1 Critical velocity for traversing

We start the discussion of our experimental results by making a qualitative description of the observed phenomena. Figure 5 shows an image sequence from two typical experiments. Upon impact of the jet onto the droplet, a cavity is generated inside the droplet. The cavity diameter and depth increase with time and its growth rate is dependent on the impact conditions [9]. At a velocity above a critical value, the jet traverses the droplet completely, as is observed in the left panel of Fig. 5. In contrast, if the jet velocity is not sufficiently large, the jet gets *embedded* in the droplet and

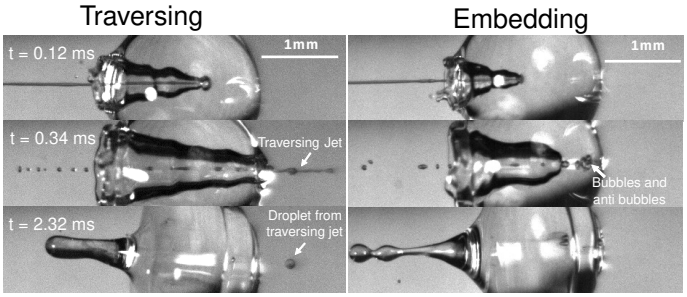

Fig. 5 Left, snapshots of a liquid jet impacting ($We_{jet} = 587$) and traversing a PEO 100k 0.1wt % droplet ($D_{drop} = 2.09$ mm). Here, we observe that the jet continues its trajectory even after going through all the droplet. Right, snapshots of a liquid jet impacting ($We_{jet} = 362$) and getting embedded in a PEO 100k 0.1wt % droplet ($D_{drop} = 2.08$ mm). During embedding, bubbles and antibubbles can be created, see movie 4 in the supplementary materials. We note that in both image sequences a rebounding Worthington jet is observed at t = 2.32 ms

bubbles and anti-bubbles may be created, as in the right panel of 5 (see also Song *et al.* 2020 [28]). Finally, and irrespective of which of these two scenarios applies a rebound Worthington jet is generated.

Now we move on to verifying the validity of the traversing criterion expressed in the critical Weber number obtained in equation (10), for varying droplet properties. To compare the experimental data and the model presented in section §3.2, we use the ratio between the experimentally obtained Weber number We_{jet} and the expected critical Weber number We_{jet}^* from equation (10). Additionally, for the droplets that contain surfactants we need to take into account that, when the jet impacts the droplet and the cavity starts to form, new surface area is created and the surface density of the surfactant decreases. Therefore, the surface tension locally increases from the surface tension measured at equilibrium and the cavity presents a *dynamic* surface tension γ_{dyn} [29]. Consequently, in the surfactant case we re-define the Weber number as $We_{dyn} = \frac{\rho_{jet}U_{jet}^2 D_{jet}}{\gamma_{dyn}}$, i.e., using γ_{dyn} in its definition, and divide it by the critical value We_{jet}^* leading to,

$$\frac{We_{dyn}}{We_{jet}^*} = \frac{We_{jet}}{We_{jet}^*}\left(\frac{\gamma_{drop}}{\gamma_{dyn}}\right) = \frac{\rho_{jet}U_{jet}^2 D_{jet}^{3/2}}{(2^{11/2})\gamma_{dyn}D_{drop}^{1/2}}. \tag{11}$$

Clearly in the above equation, for the droplets that do not contain sufactants (the glycerol solutions, water and ethanol) we just insert $\gamma_{dyn} = \gamma_{drop}$. For Triton X-100 solutions, the dynamic surface tension can be assessed by the diffusion scale T_D, which is the time for the surface tension to decrease from the surface tension of water to the equilibrium surface tension [30]. The diffusion scale depends on the diffusion coefficient of the surfactant (for Triton X-100 $\delta = 2.6\times10^{-10}$ m^2/s), the maximum surface concentration of surfactant ($\Gamma = 2.9\times10^{-6}$ mol/m^2), the Langmuir equilibrium adsorption constant ($K = 1.5\times10^3$ m^3/mol) and its volume concentration C [30,31]. For the 3 CMC Triton X-100 solution (the largest concentration used in these experiments), $T_D \sim 70$ ms, while the characteristic timescale of the traversing/embedding process is ~ 0.5 ms, i.e., two orders of magnitude smaller. Hence, the dynamic surface tension does not have enough time to reach the

View Article Online
DOI: 10.1039/D1SM00706H

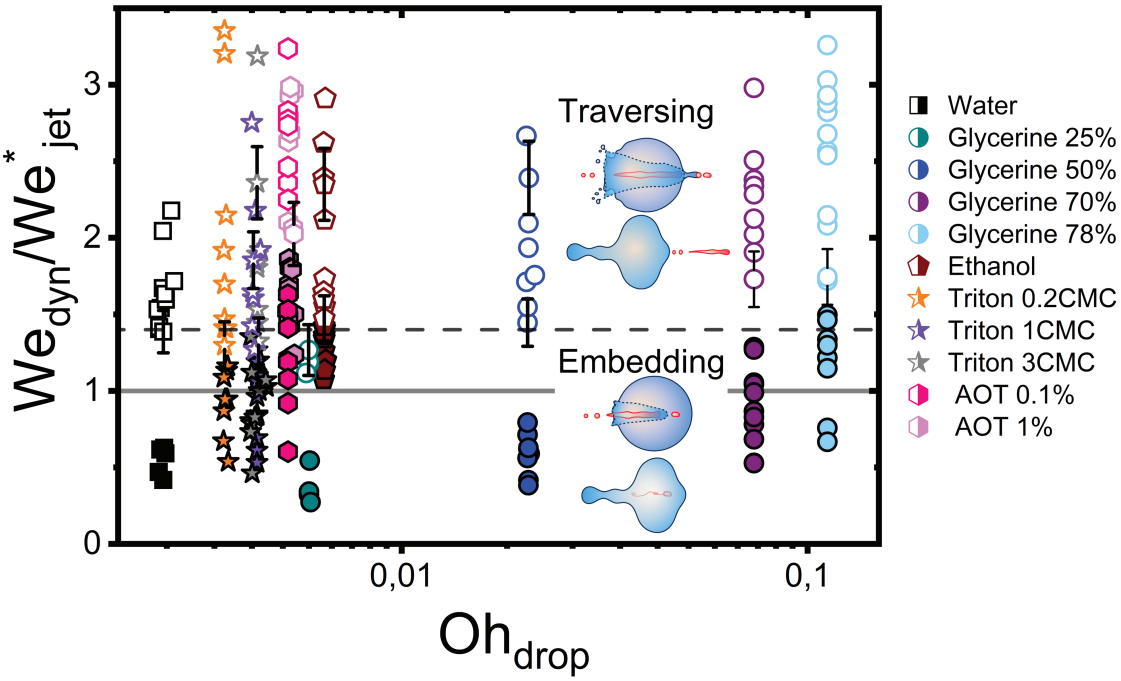

Fig. 6 Phase diagram with the rescaled Weber number We_{dyn}/We^*_{jet} on the vertical axis and the Ohnesorge number Oh_{drop} on the horizontal axis. Open symbols represent cases where the jet traverses the droplet, while solid ones stand for the embedding case. The grey line corresponds to $We_{dyn}/We^*_{jet} = 1$ and the dashed line is $We_{dyn}/We^*_{jet} = 1.4$ obtained by averaging the minimum value of observed traversing for all the liquids (excluding the AOT solutions). The experimental data is in good agreement with the model, i.e, for each liquid, most of the open symbols lie above the dashed line and conversely for closed symbols. Uncertainty was calculated for all the experimental data and example error bars are shown at selected points, where the uncertainty was found to increase linearly with the rescaled Weber number.

measured equilibrium surface tension. Therefore, we do not expect the equilibrium surface tension of Triton X-100 solutions to be relevant in the jet traversing process. Consequently, we assume the dynamic surface tension γ_{dyn} of the Triton X-100 solutions to be that of water.

In contrast, AOT being a vesicle surfactant can migrate faster than micelle surfactants such as Triton X-100[32,33]. In addition, it was shown that at ~ 10 ms the dynamic surface tension of an AOT solution at 1 wt. % can decrease to a value of ~ 32 mN/m[32]. Therefore, we assume that γ_{dyn} for the AOT solutions is ~ 32 mN/m. We should note however, that AOT dynamics are more complex than those of Triton, and characterisation using a single time scale is an oversimplification.

Figure 5 shows the experimental results of traversing and embedding impact cases as a phase diagram, where on the vertical axis we plot the ratio of the (dynamic) Weber number We_{dyn} and the expected critical Weber number We^*_{jet}, using equation (11) such that based upon the model described in §3.2 we would expect a transition at $We_{dyn}/We^*_{jet} = 1$. On the horizontal axis we separate the liquid properties of the droplet by plotting the Ohnesorge number, defined as $Oh_{drop} = \mu_{drop}/\sqrt{\rho_{drop} D_{drop} \gamma_{drop}}$, which is the ratio between viscous forces to inertial and surface tension forces, and has the advantage that is a material property, i.e., it is independent of the dynamics. Open symbols in Fig. 5 represent cases where the jet was observed to traverse the droplet, (as in Fig. 5 left) and solid symbols represent the situation where the jet does not traverse the droplet, i.e., becomes embedded as seen in Fig. 5 right.

From Fig. 6, we observe that most of the open symbols lie above the same approximate value ~ 1.4 and conversely for closed symbols. The exception is formed by the data for the AOT solutions, where it is possible that γ_{dyn} is underestimated as $\gamma_{dyn} \approx 32.2$ mN/m, and in fact lies closer to the surface tension of water 72.1 mN/m. An accurate measurement of the dynamic surface tension in such timescales is challenging[29,34] and is out of the scope of this work. However, as demonstrated by our results, the dynamic surface tension can play a pronounced role for different dynamic conditions. Therefore, we can safely conclude that the impact process is initially dominated by inertia and that surface tension is the major opposing force.

Turning to the viscoelastic droplets, Fig. 7b shows data for the jet traversing and embedding impact cases for droplets consisting of the PEO solutions. In this figure, we plot We_{dyn}/We^*_{jet} against the Deborah number defined as $De = \lambda/\tau_c$, where λ is the relaxation time of the polymer (see table 1) and $\tau_c = (\rho_{drop} D^3_{drop}/\gamma_{drop})^{1/2}$ is the capillary timescale. We use this definition of the Deborah number to our PEO solution droplets, as we expect to observe deviations from the Newtonian behaviour when λ becomes comparable to the scale at which surface tension starts to influence the cavity dynamics, i.e., at the capillary time scale τ_c. In Fig. 7, open and closed symbols again represent traversing and embedding cases respectively and half-filled symbols denote an intermediate state between traversing and embedding, which we call *pearling*. During pearling, the jet travels a distance larger than D_{drop} after impact and thus protrudes from the droplet, but due to the viscoelastic properties of the liquid gets sucked back

View Article Online
DOI: 10.1039/D1SM00706H

into the droplet, as visualised in the experimental snapshots of Fig. 7a.

From Fig. 7b that the traversing and embedding process for the PEO solutions with $De \lesssim 4 \times 10^{-3}$, is similar for Newtonian liquids, leading to the same threshold value We^*_{jet}, showing that the viscoelastic effects are weak. However, as De increases, i.e., when the viscoelastic timescales become increasingly comparable to the capillary time, the jet needs larger speeds to traverse the droplet. This is in line with previous experiments where by increasing the elastic modulus of gelatin the cavity depth of an impacting sphere would decrease, keeping the impact velocity constant[35]. These results show that viscoelastic properties as described by De significantly change the traversing dynamics. This is crucial information when trying to understand needle-free injections on skin, as it has been shown that skin has viscoelastic properties[36]. However, conducting systematic studies trying to quantify the influence of skin properties during injection processes is challenging, because of high variability from person to person and even between different parts of the body[36,37]. Furthermore, studying the viscoelastic properties of skin is in itself challenging given the opacity of skin[38,39]. In this context, our results present information about the characteristics of the impact with a simpler system than skin, isolating the effects of individual material properties of the target from the enormous complexity of skin.

4.2 Cavity dynamics

To obtain more insight into the dynamics of the cavity that is created in the droplet, we studied the cavity velocity in the positive x direction, i.e., while the jet is penetrating into the droplet, as sketched in Fig. 8a. For each liquid we plot the average ratio of the cavity velocity U_c and the jet velocity U_{jet} (bold symbols), together with the values obtained for each individual experiment (light symbols) as a function of Oh_{drop} in Fig. 8c. The measured and averaged values are remarkably close to the value $U_c/U_{jet} = 0.5$, which is to be expected for the impact of a continuous jet on a pool, and is in agreement with previous works[2]. The slight deviation observed for the water and the PEO solutions droplets, could be due to water and PEO solution droplets being the largest ones used in the experiments. In that case, the breakup of the jet could influence U_c, similarly to a train of droplets impacting a deep pool[8,9].

In addition to U_c, we measured the retraction cavity velocity U_{cr} after the cavity reached its maximum length, as sketched in Fig. 7b. In Fig. 8d, we show U_{cr} rescaled by the capillary velocity scale $U_\gamma = \sqrt{\gamma_{dyn}/\rho_{drop} D_{drop}}$. We observe that the average of data for the different liquids are similar, taking into consideration the data dispersion. The average of ethanol, water and aqueous glycerol mixtures are even statistically indistinguishable, given the error margins of the experiment. The lower average values of U_{cr} for the AOT and Triton solutions can possibly be explained by the Marangoni stresses generated by the flow from areas with low surface tension to those with high surface tension. Indeed, Marangoni stresses have been shown to retard cavity collapse and slow the velocity of Worthington jets[40,41]. Therefore, we can assume that $U_{cr} \propto U_\gamma$, indicating that the retraction of the cavity is

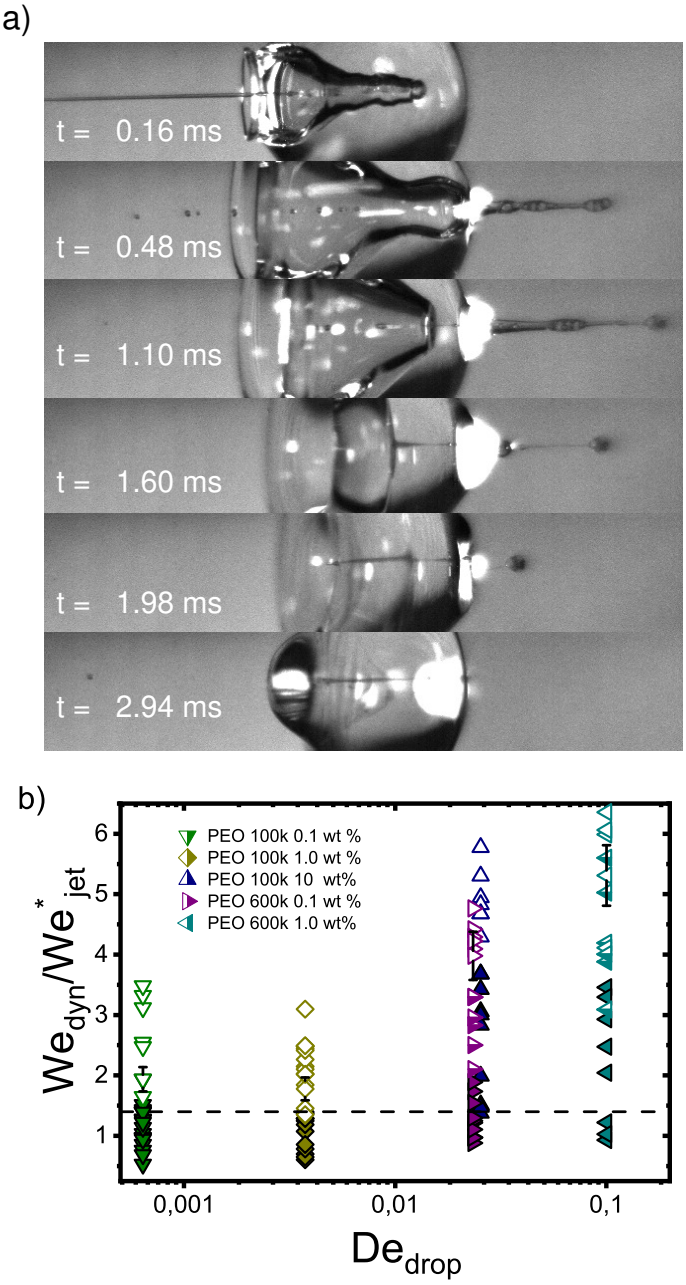

Fig. 7 a) Snapshots of a liquid jet impacting a water droplet with PEO 600k 1 wt% showing pearling (see movie 5 in the supplementary materials). A jet with $U_{jet} = 33.5$ m/s and $We_{jet} = 1160$ impacts a droplet with $D_{drop} = 2.21$ mm. The jet travels a distance larger than D_{drop}, but due to the viscoelastic effects of the droplet, it gets sucked back into the droplet. b) Phase diagram in terms of De and We^*_{dyn}. Open symbols represent cases where the jet traverses the droplet, solid ones stand for the embedding case and half filled ones represent pearling. The dashed line represents the transition from traversing to embedding cases observed for Newtonian liquids. Uncertainty was calculated for all the experimental data and example error bars are shown at selected points, where the uncertainty was found to increase linearly with We_{dyn}/We^*_{jet}.

View Article Online
DOI: 10.1039/D1SM00706H

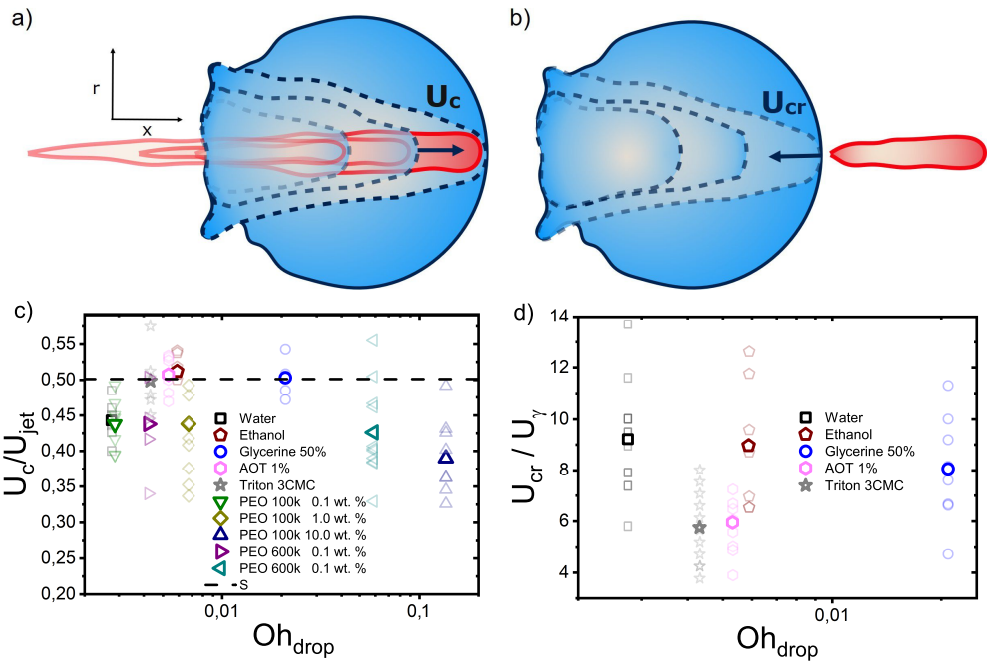

Fig. 8 Sketch illustrating the definitions of a) the cavity velocity U_c and b) the velocity of the retracting cavity U_{cr}. c) Ratio of the cavity velocity U_c and the impact velocity U_{jet}, compared to the expected value 0.5. d) U_{cr} divided by the capillary velocity scale $U_\gamma = \sqrt{\gamma_{dyn}/\rho_{drop}D_{drop}}$; average values for each liquid are statistically similar, indicating that the retraction of the cavity is governed by capillary forces. For each liquid, bold coloured symbols represent average values of light symbols.

surface tension driven[42]. The origin of the dispersion in U_{cr} is associated with the jet tail breakup, where the matryoshka effect or the creation of an antibubble may arise, like in Fig. 5[28,29].

4.3 Observations after the cavity collapse

After the retraction phase, the cavity collapses and generates a Worthington jet (as e.g., depicted in the last panel of Fig. 3). Extensive studies of the length, speed and breakup time of a Worthington jet formed after droplet and solid impact on a liquid pool have been widely reported, and are outside of the scope of this paper[1,40,42–47]. Moreover, given the random breakup of the impacting jet in our experiments, the Worthington jets are observed to vary widely in size and shape, even when droplet and impacting jet consist of the same liquids. This is understandable, as it has been shown in the literature that small disturbances in the cavity can have a strong influence on the Worthington jet properties[42].

Lastly, we observe that the mixing and diffusion of the impacting jet into the droplet is governed by the droplet characteristics. Indeed, for a jet impacting a water droplet with AOT 0.1 wt% below the critical value U^*_{jet} needed for traversing, there is vortical mixing (Fig. 9 left). Comparable mixing patterns were observed (data not shown) for the rest of the Newtonian liquids containing surfactants, and weaker mixing is seen for water, ethanol and glycerine 25 % droplets. Similar mixing patterns have been described in the literature, for example, Jia *et al.* in 2020[40] reported an interfacial Marangoni flow enhancing the mixing of an impacting droplet and a liquid pool with different surface tensions.

We note that in our experiments the surface tension of the jet is almost always expected to be different from the surface ten-

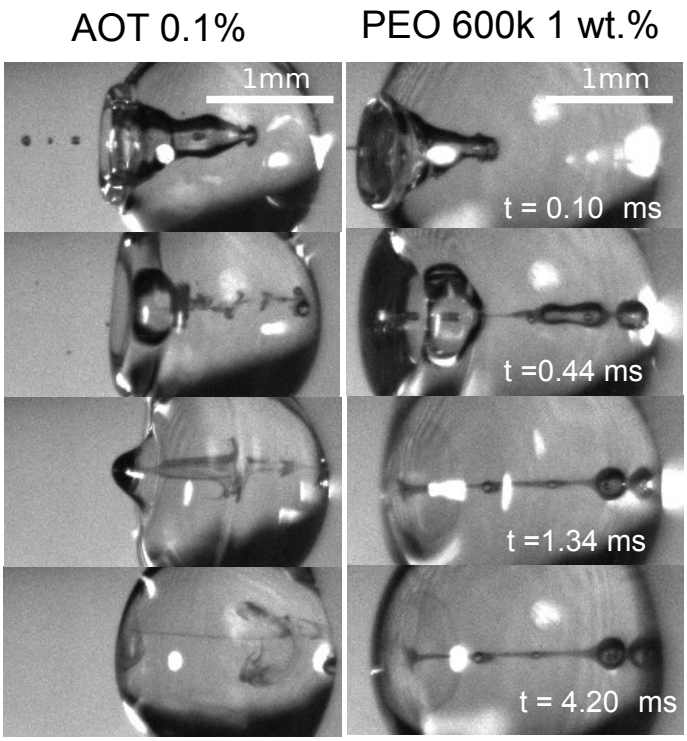

Fig. 9 Mixing after impact and cavity collapse. Left, jet impacting an AOT 0.1 wt.% droplet with $We_{jet} = 359$. In the sequence we observe vortical mixing presumably due to the Marangoni flow caused by the difference of surface tension between the jet and the droplet (see movie 6 in the supplementary materials and Jia *et al.* 2020[40]). Right, jet impacting a PEO 600k 1 wt.% with $We_{jet} = 574$. In this sequence we observe little mixing and diffusion due to the viscoelastic properties of the droplet even after 0.42 ms.

sion of the droplet, and a Marangoni flow could explain this type of mixing. However, a more in depth study is needed to confirm this hypothesis. In contrast, for the viscoelastic liquids with $De \gtrsim 2 \times 10^{-2}$ and the glycerol mixture liquids with $Oh \gtrsim 0.02$, the jet does not mix with the droplet in the timescale of our experiments (Fig. 9b). Furthermore, low viscosity ($Oh \lesssim 0.01$) and low surface tension liquids reach equilibrium at a later stage than more viscous liquids ($Oh \gtrsim 0.02$) and with higher surface tension. For example, in Fig. 9 a PEO 600k 1 wt.% droplet reaches equilibrium ~ 4 times faster than the AOT droplet. This is expected, as surface tension and viscosity have been observed to affect droplet oscillations [48,49].

5 Conclusions

We have presented experimental results of liquid water jets impacting on pendant droplets with different liquid properties. We proposed two models to predict a critical jet impact velocity beyond which the jet traverses the droplet. First, we presented a model based on a simple energy balance between the jet kinetic energy and the change in surface tension of the droplet. The second model is based on the comparison between the Young-Laplace and the dynamic pressures of the cavity made by the penetrating jet, and its shape is described by the two-dimensional Rayleigh equation.

Although the critical velocity predicted in both models is of the same order of magnitude, they differ in their scaling relation with D_{drop}/D_{jet}. The difference arises from the different description of the cavity geometry and its associated surface energy. In the energy balance model, a cylindrical shape is assumed, contrasting with the more accurate cavity shape described by the two-dimensional Rayleigh equation. Furthermore, we tested the validity of the second model, by fitting our experimental data with equation (11), showing good agreement when dynamic surface tension effects are considered, see Fig. 6. Therefore, for Newtonian droplets the impact process is initially dominated by inertia and their dynamic surface tension is the major opposing force.

In addition, we investigated viscoelastic effects by using water-based polyethylene-oxide solutions of varied concentrations and molecular weight. For $De \lesssim 4 \times 10^{-3}$, the droplets act as if they were Newtonian. In contrast, for $De \gtrsim 2 \times 10^{-2}$, a greater jet impact speed is necessary to traverse the droplet, indicating that when the capillary and relaxation times are comparable, viscoelastic effects can dominate the traversing phenomena. Moreover, we observed a distinct transition phenomenon from traversing to embedding, which we called pearling and on which the protruing jet is sucked back into the droplet.

Next, we investigated the advancing and retraction velocities U_c and U_{cr} of the cavity, confirming previous reports that $U_c/U_{jet} \sim 0.5$ for different liquids. Furthermore, we found that U_{cr} is surface tension driven, with the connotation that for droplets containing surfactants U_{cr} is observed to be slower than for the other liquids that were used, which could be explained by Marangoni stresses.

Our results are relevant for needle-free injections into soft tissues other than skin, e.g. the eye, where controlling the jet velocity, U^*_{jet} would be essential to avoid undesired tissue damage and ensure successful drug delivery.

Author contributions

M.A.Q.S, D.v.d.M. and D.F.R conceived the experiments, analysed the results and wrote the manuscript. M.A.Q.S and D.F.R designed and built the experimental setup. M.A.Q.S performed the experiments. I.W.H participated in the discussions and wrote the manuscript.

Conflicts of interest

There are no conflicts to declare.

6 Acknowledgements

This research was funded by the European Research Council (ERC) under the European Union Horizon 2020 research and innovation programme (Grant agreement No. 851630). We thank valuable discussions with Loreto Oyarte-Gálvez, Javier Rodríguez-Rodríguez, Álvaro Marín, Ivo Peters and Detlef Lohse. We also thank Ambre Bouillant and Ali Rezaei for their assistance on the shear viscosity measurements. The guidance of James W. Bales and Andrew Davidhazy through Edgerton's Digital Collection was of great value. David Fernandez Rivas, would like to thank Gareth McKinley for his input at the start of the project and for hosting his stay at the HML and the MIT.

Notes and references

1 A. M. Worthington, *A study of splashes*, Longmans, Green, and Company, 1908.
2 H. N. Oguz, A. Prosperetti and A. R. Kolaini, *Journal of Fluid Mechanics*, 1995, **294**, 181–207.
3 M. Lee, R. Longoria and D. Wilson, *Physics of Fluids*, 1997, **9**, 540–550.
4 Y. Zhu, H. N. Oğuz and A. Prosperetti, *Journal of Fluid Mechanics*, 2000, **404**, 151–177.
5 É. Lorenceau, D. Quéré and J. Eggers, *Physical Review Letters*, 2004, **93**, 254501.
6 J. M. Aristoff and J. W. Bush, *Journal of Fluid Mechanics*, 2009, **619**, 45–78.
7 T. T. Truscott, B. P. Epps and J. Belden, *Annual Review of Fluid Mechanics*, 2014, **46**, 355–378.
8 W. Bouwhuis, X. Huang, C. U. Chan, P. E. Frommhold, C.-D. Ohl, D. Lohse, J. H. Snoeijer and D. van der Meer, *Journal of Fluid Mechanics*, 2016, **792**, 850–868.
9 N. B. Speirs, Z. Pan, J. Belden and T. T. Truscott, *Journal of Fluid Mechanics*, 2018, **844**, 1084.
10 H. E. Edgerton, *Electrical Engineering*, 1931, **50**, 327–329.
11 M. R. Prausnitz, S. Mitragotri and R. Langer, *Nature Reviews Drug discovery*, 2004, **3**, 115–124.
12 N. C. Hogan, A. J. Taberner, L. A. Jones and I. W. Hunter, *Expert Opinion on Drug Delivery*, 2015, **12**, 1637–1648.
13 A. Mohizin and J. K. Kim, *Journal of Mechanical Science and Technology*, 2018, **32**, 5737–5747.
14 S. F. Rastopov and A. T. Sukhodolsky, Optical Radiation Interaction with Matter, 1991, pp. 127–134.
15 J. Padilla-Martínez, C. Berrospe-Rodriguez, G. Aguilar,

J. Ramirez-San-Juan and R. Ramos-Garcia, *Physics of Fluids*, 2014, **26**, 122007.

16 C. B. Rodríguez, C. W. Visser, S. Schlautmann, D. F. Rivas and R. Ramos-Garcia, *Journal of Biomedical Optics*, 2017, **22**, 105003.

17 L. Oyarte Gálvez, A. Fraters, H. L. Offerhaus, M. Versluis, I. W. Hunter and D. Fernández Rivas, *Journal of Applied Physics*, 2020, **127**, 104901.

18 K. Cu, R. Bansal, S. Mitragotri and D. F. Rivas, *Annals of Biomedical Engineering*, 2019, 1–12.

19 L. Oyarte Gálvez, M. Brió Pérez and D. Fernández Rivas, *Journal of Applied Physics*, 2019, **125**, 144504.

20 A. Daerr and A. Mogne, *Journal of Open Research Software*, 2016, **4**, e3.

21 M. Grotte, F. Duprat, D. Loonis and E. Piétri, *International Journal of Food Properties*, 2001, **4**, 149–161.

22 T. Truscott, A. Techet and D. Beal, *Proceedings of the International Symposium on Cavitation*, 2009.

23 G. Birkhoff, D. P. MacDougall, E. M. Pugh and S. G. Taylor, *Journal of Applied Physics*, 1948, **19**, 563–582.

24 K. T. Kiger and J. H. Duncan, *Annual Review of Fluid Mechanics*, 2012, **44**, 563–596.

25 Q. Deng, A. Anilkumar and T. Wang, *Journal of Fluid Mechanics*, 2007, **578**, 119–138.

26 R. Bergmann, D. van der Meer, M. Stijnman, M. Sandtke, A. Prosperetti and D. Lohse, *Physical Review Letters*, 2006, **96**, 154505.

27 J. Eggers, M. Fontelos, D. Leppinen and J. Snoeijer, *Physical Review Letters*, 2007, **98**, 094502.

28 Y. Song, L. Zhang and E. N. Wang, *Physical Review Fluids*, 2020, **5**, 123601.

29 N. Speirs, M. Mansoor, R. Hurd, S. Sharker, W. Robinson, B. Williams and T. T. Truscott, *Physical Review Fluids*, 2018, **3**, 104004.

30 A. Bobylev, V. Guzanov, A. Kvon and S. Kharlamov, Journal of Physics: Conference Series, 2019, p. 012073.

31 J. K. Ferri and K. J. Stebe, *Advances in Colloid and Interface Science*, 2000, **85**, 61–97.

32 M. Song, J. Ju, S. Luo, Y. Han, Z. Dong, Y. Wang, Z. Gu, L. Zhang, R. Hao and L. Jiang, *Science Advances*, 2017, **3**, e1602188.

33 T. Wang, Y. Si, S. Luo, Z. Dong and L. Jiang, *Materials Horizons*, 2019, **6**, 294–301.

34 N. J. Alvarez, L. M. Walker and S. L. Anna, *Langmuir*, 2010, **26**, 13310–13319.

35 A. Kiyama, M. M. Mansoor, N. B. Speirs, Y. Tagawa and T. T. Truscott, *Journal of Fluid Mechanics*, 2019, **880**, 707–722.

36 Y.-c. Fung, *Biomechanics: mechanical properties of living tissues*, Springer Science & Business Media, 2013.

37 H. Joodaki and M. B. Panzer, *Proceedings of the Institution of Mechanical Engineers, Part H: Journal of Engineering in Medicine*, 2018, **232**, 323–343.

38 M. L. Crichton, B. C. Donose, X. Chen, A. P. Raphael, H. Huang and M. A. Kendall, *Biomaterials*, 2011, **32**, 4670–4681.

39 H. K. Graham, J. C. McConnell, G. Limbert and M. J. Sherratt, *Experimental Dermatology*, 2019, **28**, 4–9.

40 F. Jia, K. Sun, P. Zhang, C. Yin and T. Wang, *Physical Review Fluids*, 2020, **5**, 073605.

41 C. Constante-Amores, L. Kahouadji, A. Batchvarov, S. Shin, J. Chergui, D. Juric and O. Matar, *Journal of Fluid Mechanics*, 2021, **911**, A57.

42 G.-J. Michon, C. Josserand and T. Séon, *Physical Review Fluids*, 2017, **2**, 023601.

43 J. Cheny and K. Walters, *Journal of Non-Newtonian Fluid Mechanics*, 1996, **67**, 125–135.

44 S. Gekle and J. M. Gordillo, *Journal of Fluid Mechanics*, 2010, **663**, 293.

45 Z. Che and O. K. Matar, *Soft Matter*, 2018, **14**, 1540–1551.

46 A. Mohammad Karim, *Physics of Fluids*, 2020, **32**, 043102.

47 D. Kim, J. Lee, A. Bose, I. Kim and J. Lee, *Journal of Fluid Mechanics*, 2021, **906**, A5–1–A5–14.

48 J. Kremer, A. Kilzer and M. Petermann, *Review of Scientific Instruments*, 2018, **89**, 015109.

49 J. Arcenegui-Troya, A. Belman-Martínez, A. Castrejón-Pita and J. Castrejón-Pita, *Review of Scientific Instruments*, 2019, **90**, 095109.